Marco-Gimeno, J.; Asztalos, KJ.; Moon, CY.; Powell, CF.; Marti-Aldaravi, P.; Nocivelli, L. (2024). Breakup dynamics in a pressure-swirl injector for urea-water solution applications: A computational study. International Journal of Engine Research. https://doi.org/10.1177/14680874241286206

Marco-Gimeno, J., Asztalos, K. J., Moon, C. Y., Powell, C. F., Martí-Aldaraví, P., & Nocivelli, L. (2024). Breakup dynamics in a pressure-swirl injector for urea-water solution applications: A computational study. International Journal of Engine Research. https://doi.org/10.1177/14680874241286206

Breakup Dynamics in a Pressure-Swirl Injector for Urea-Water Solution Applications: A Computational Study.

Author List

Javier Marco Gimeno[1], Katherine J. Asztalos[2], Chi Young Moon[2], Christopher F. Powell[2], Pedro Martí-Aldaraví[1], Lorenzo Nocivelli[2].

Research institute

[1] CMT-Motores Termicos, Universitat Politecnica de Valencia, Spain

[2] Transporation and Power Systems Division, Argonne National Laboratory, USA.

ABSTRACT

The co-optimization of in-cylinder combustion and after-treatment technology has become a major aspect in engine design and development, with the goal of meeting the increasingly restrictive emission regulations in the transportation industry. Selective Catalytic Reduction is a robust technology to control the emission of NO_x, and the injection of urea in water solution is the exhaust tailpipe is a key aspect of its operation. The proposed work uses high-fidelity Computational Fluid Dynamics to characterize the atomization dynamics of the liquid jet in relevant cross-flow conditions. The study focuses on a commercial low-pressure (9 bar) pressure-swirl injector which is characterized in its internal geometry through high-resolution X-ray micro-computational tomography. The internal two-phase flow has been modeled according to the volume-of-fluid approach in a large eddy simulation framework and validated against near-nozzle X-ray radiography measurement. Moreover, characterizing the breakup dynamics for the swirling hollow cone formation, and assessing the influence of the cross-flow in the breakup dynamics was completed. The results have been reported proposing Re-Oh maps and probability density functions of the spray kinematics. Higher cross-flow momentum generates an increase in the jet intact length and a reduction of the liquid droplet diameters. The axial momentum of the jet is affected by the cross-flow already in the near-nozzle region, determining a relevant deviation of the spray velocities. This work aims to inform the initialization of Eulerian-Lagrangian spray models through informed initialization of droplet diameters and static one-way coupling between volume-of-fluid results and Lagrangian spray parcels, to be used for system-size domain simulations.

KEYWORDS

Urea-Water-Solution, Swirling Flow, Adaptive Mesh Refinement, Large Eddy Simulation, cross-flow, CONVERGE

LIST OF NOTATION

t Time

xi Direction in each space coordinate

A Area of the nozzle section

S Source term

P Pressure

u X-Component of velocity

v Y-Component of velocity

w Z-Component of velocity

p Scale parameter

k Kinetic energy

L_{ref} Length of refined cell

L_{base} Length of the base cell

SN Swirl Number

J Momentum ratio

t Thickness

C_a Area Coefficient

$\dot{M}$ Momentum of the liquid jet

$\dot{m}$ Mass Flow Rate of the liquid jet

We Weber Number

Re Reynolds Number

GREEK SYMBOLS

α Volumetric Void Fraction

ρ Density

ν_{SGS} Sub-Grid Viscosity

Δ_e Filter Length

μ Dynamic Viscosity

ABBREVIATIONS

AMR Adaptive Mesh Refinement

LES Large-Eddy-Simulation

CFD Computational Fluid Dynamics

NO_x	Nitrogen Oxides
SCR	Selective Catalytic Reduction
UWS	Urea-Water Solution
SMD	Sauter Mean Diameter
VOF	Volume of Fluid
SGS	Sub-Grid Scale
TKE	Turbulent Kinetic Energy
IL	Intact Length
FR	Fixed Refinement
CT	Computerized Tomography
TIM	Transverse Integrated Mass

1. INTRODUCTION

The awareness of the emissions of combustion products has increased due to the continuously rising demand of vehicles for transportation purposes [1]. Nitrogen Oxide (NOx) is one of the main components of harmful emissions from both Compression-Ignited (CI) and Spark-Ignited (SI) engines. [2] [3] [4]. Hence, the trend in emission regulations has been to restrict the amount of such gases that can be emitted into the atmosphere [7] . In addition, in novel engines, the problem of these emissions is not entirely mitigated, as NOx are not only produced from traditional fuels, but they also appear in other technologies such as in hydrogen combustion processes [5] and ammonia [6]. One of the main technologies capable of significantly reducing the NOx is Selective Catalytic Reduction (SCR), which abates the NOx into nitrogen and water through the combination of the harmful gases and ammonia. As storing ammonia introduces safety and toxicological issues [8], a spray of Urea-Water Solution (UWS) is injected in the exhaust line, which due to the thermolysis and hydrolysis process, transforms into the required ammonia [9]. UWS is commonly composed of 32.5% by weight urea and is injected immediately upstream of the reduction catalyst for conversion into ammonia. Without careful design and control, the injection process could lead to wall-impingement onto the exhaust walls with the possibility of deposit formation [10] that could affect the after-treatment performance [11] and the fuel economy by increasing the system back-pressure [12]. Hence, improving atomization and understanding how these sprays work are key aspects for further development of this technology.

Numerous efforts have been done toward this objective in both experimental and computational fields. Experimentally, several studies have been performed to understand the spray characteristics. Kalyankar et al. [13] employed several optical techniques such as High-Speed Shadowgraphy (HSS), Laser Diffraction (LD), Laser Sheet Imaging (LSI), Laser Doppler Velocimetry (LDV), and Phase Droplet Anemometry (PDA) to a commercial pressure-swirl UWS injector under quiescent conditions, showing similar results for the velocity correlations and differences on the profiles of mass flow, velocity and Sauter Mean Diameter (SMD). Analysis of the breakup length of a UWS injector under typical injection pressure was done by Kapusta et al. [14] using both pure water and UWS as the working fluid. The effect of different working liquids was mainly shown through the breakup length evolution, showing an average intact length value of 6 mm and 5.5 mm for UWS and pure water, respectively. Nonetheless, substituting UWS with pure water is a common practice when researching the behavior of such low injection pressure sprays [15]–[17]. Moon et al. [18] also used water as the working fluid, acquiring projected mass density on a pressure-swirl UWS injector under cross flow conditions using focused-beam X-ray radiography. On the computational side, the most common practice to recreate UWS sprays is the Lagrangian-Eulerian approach, in which the liquid phase is represented by a cluster of droplets that share the same fluid-dynamic characteristics, and their position and trajectory are tracked through the computational domain, while the gas phase is represented by the cells in which the domain has been discretized. This allows for a representation of the spray in the far-field region. For example, Payri et al. [19] validated an inert model against experimental data obtained using diffused back illumination (DBI). The far-field characteristics of the spray such as the angle, the spatial discretization of the SMD and the evolution of the penetration for a range of different injection pressures were identified. Due to the low Weber numbers associated with the jet and the injected droplets, it is mandatory for such models to introduce a droplet distribution function to represent the outcomes of the primary breakup phenomenon [19]–[22], This is usually represented by means of a Rosin-Rammler distribution or an experimentally extracted profile. For the same reason, no secondary droplet breakup is usually expected for such applications [23]. To be able to predict the jet primary breakup with a droplet distribution, another approach needs to be utilized. The Eulerian-Eulerian framework, although considerably more expensive, allows for extracting such information from the simulations. This approach, commonly known as Volume-Of-Fluid (VOF), has been employed in several studies for gasoline injectors, such as works by Chen et al. [24] and Ishimoto et al. [25], in which the primary breakup of a gasoline jet was predicted. Very little work utilizing VOF for UWS injectors has been conducted. Payri et al. [26] used a Mixture Model approach to validate the experimental mass flow rate of a three-hole UWS injector and assess the differences between the three orifices. However, Edelbauer et al. [27] applied a VOF approach to a three-hole UWS injector. Due to the computational cost of the Eulerian-Eulerian simulations, only

one jet out of three was considered. A Fixed Refinement (FR) procedure was followed, reaching a cell count of 114 million to properly detect the breakup mechanisms of the mixture. Anticipating the need to initialize the DDM models for UWS sprays with pre-defined data, they were able to couple such VOF simulation with a DDM simulation to capture both the near and far-field characteristics of the spray.

To the authors' best knowledge, there is a lack of studies focused on characterizing the primary breakup processes of after-treatment sprays. Specifically, there is a lack of validation of CFD simulations in the very near vicinity – less than 5 mm from the injector tip – which we were able to obtain leveraging X-ray radiography data. The present study presents the computational analysis of a single-hole pressure-swirl atomizer, which is operated at realistic injection pressures and in the presence of gaseous cross-flows representative of exhaust after-treatment channels. The internal geometry of the injector is resolved to the micron scale utilizing X-ray micro-tomography, which enables high-fidelity characterization of the liquid internal flow generating the hollow conical liquid jet. Moreover, distinct from most studies available in literature, which are performed using fixed-refinement (FR) meshes for their simulations, this research aims to add knowledge to the after-treatment community by characterizing a UWS pressure-swirl injector with a VOF framework and by applying a meshing methodology known as Adaptive Mesh Refinement (AMR) to significantly reduce the total cell count and develop an efficient computational framework for studying these injectors. The paper is structured as follows: section 2 describes the numerical methods and setup used for simulation of the injection and liquid jet breakup; section 3 describes the injector used in the study, and section 4 reports the validation of the simulation and the key findings. We characterized the atomization regime of the hollow cone jet at different gas cross-flow rates, and analyzed the breakup length and atomization outcomes in terms of particle kinematics. The paper is aimed at providing insight into the atomization process and to produce guidelines to initialize spray models and improve the fidelity of system-level simulations of SCR pre-catalytic sections.

2. NUMERICAL METHODS

The simulations have been carried out with the commercial CFD software CONVERGE (v3.0)[28]. Both gas and liquid phases are discretised and solved according to the Eulerian framework, in which the Volume-Of-Fluid method is implemented into a single-fluid multi-phase approach. The transport equations of mass transport (1) and momentum (2) are complemented with the transport of the volumetric void fraction (3). In the reported formulation, the void fraction (α) is the ratio of gas volume inside a cell with the total volume of the same cell (4). Therefore, α is a continuous variable ranging between $\alpha = 0$, representative of a cell filled with liquid, and $\alpha = 1$ representative of a cell filled with gas.

$$\frac{\partial \rho}{\partial t} + \frac{\partial \rho u_i}{\partial x_i} = S$$	(1)
$$\frac{\partial \rho u_i}{\partial t} + \frac{\partial \rho u_i u_j}{\partial x_j} = -\frac{\partial P}{\partial x_i} + \frac{\partial \sigma_{ij}}{\partial x_j} + S$$	(2)
$$\frac{\partial \alpha}{\partial t} + u \cdot \nabla \alpha = 0$$	(3)
$$\alpha = \frac{V_{gas}}{V_{cell}}$$	(4)

In the VOF formulation, density and viscosity of each cell are computed according to Equation (5) and Equation (6), respectively.

$$\rho = \rho_{gas}\alpha + \rho_{liquid}(1-\alpha) \quad (5)$$

$$\mu = \mu_{gas}\alpha + \mu_{liquid}(1-\alpha) \quad (6)$$

A pressure-based method is used to solve the Navier-Stokes equations. The pressure-velocity coupling is based on the Pressure Implicit with Splitting of Operator (PISO) algorithm [29]. The Rhie-Chow scheme [30] has been applied to avoid the checkerboard effect. The momentum and pressure equations have been solved with the Biconjugate Gradient Stabilized Method (BICGSTAB) [31].

Since α is a continuous variable, the High-Resolution Interface Capturing (HRIC) algorithm [32] is chosen to reconstruct and identify the liquid-gas interphase and eventually provide insight into the droplets and ligament formation. Turbulence is handled according to the Large Eddy Simulation (LES) formulation, using the Dynamic Smagorinsky model [33] for subgrid eddies, which is a modification from the traditional Smagorinsky model that determines the local value of the model coefficient by means of the Germano identity to model the subgrid-scale structures. The choice of using a subgrid scale model is motivated by the choice of adaptive mesh refinement, which dynamically increases the resolution of the grid as a function of secondary derivatives of velocity and void-fraction. The Werner and Wengle wall model [34] is used on the geometry walls since the refinement near the walls does not allow for the solution of the boundary layer dynamics.

2.1 INJECTION HARDWARE MODEL

The presented work focuses on a commercially available pressure-swirl atomizer for after-treatment applications. The geometry of the physical unit has been scanned and reconstructed through high-resolution X-Ray micro-computed tomography (CT) performed at the Advanced Photon Source (APS) of Argonne National Laboratory [18], [35]. This

enables measurements and reproduction of micron-scale details of the internal surface and manufacturing imperfections which showed a strong influence on liquid atomization, as highlighted by Yue et al. [35]. The resulting geometry of the micro-CT has been introduced into the computational framework to perform the desired simulations. The simulation campaign covers the injection in quiescent and two cross-flow conditions. For the former, a hemispheric domain with a radius of 20 mm is coupled with the injector. In the cross-flow simulations, in order to recreate the conditions of the experimental campaign [18], a parallelepiped shape was attached to the nozzle exit with a 50.8 x 25.4 mm cross-sectional area. The computational domain has been discretised in elements with a base size of 480 µm and refined to a minimum size of 15 µm in the internal geometry of the injector, as shown in Figure 1. AMR tracking subgrid scale 2nd derivatives of void fraction and velocity, is used in the chamber/channel regions to optimize the cell count and ensure a minimum mesh size of 15 µm at the liquid-gas interface. As a result, a maximum cell count of ~80 million and ~30 million is obtained for the crossflow and the quiescent simulations, respectively. Figure 1 shows the computational grid inside the injector (a) and in the open chamber (b) for the quiescent case at quasi-steady injection conditions.

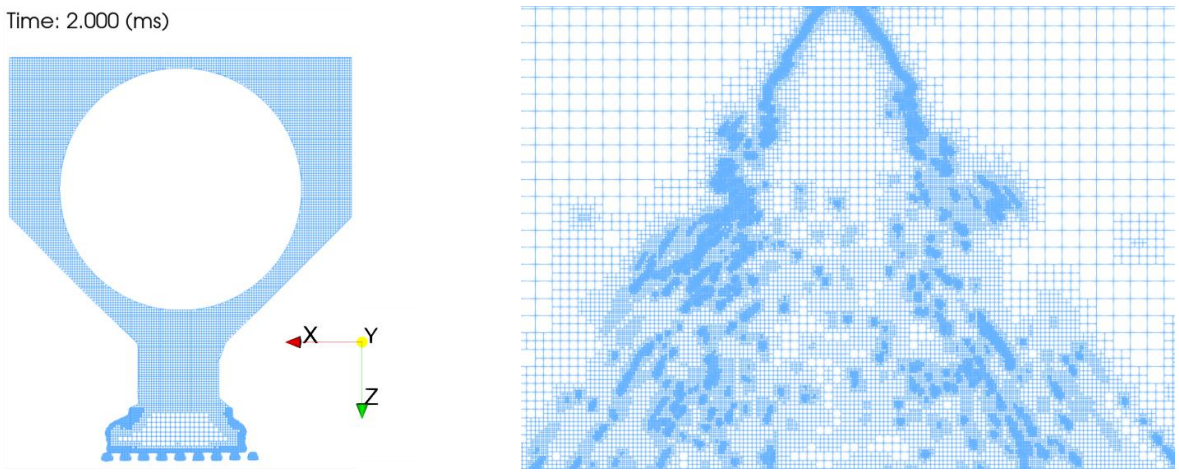

(a) Inside the injector (b) Discharge volume

Figure 1. Slices taken in X-Z plane of (a) mesh development inside the injector and (b) mesh development in the outlet boundary as shown at progressive timesteps as the flow field develops.

The system operating conditions replicate the experimental setup [18]. The injection pressure is set to 9 bar through a total pressure inflow boundary condition. The hemispheric outlet boundary of the domain is handled under a pressure-outlet condition, with a value of 1.01325 bar. Since the X-ray radiography data is available in the axial coordinate up to 15 mm from the injector tip, the chamber height has been halved in this direction to reduce the simulation cost, resulting in a 50.8 x 50.8 x 25.4 mm domain, and adapting the air mass flow rate accordingly. The resulting cross-flow velocity profile in the region of interest for the jet breakup dynamics is not affected by the bottom wall boundary layer effect, as

assessed by preliminary simulations. The gaseous cross-flow is initialized with a fully developed turbulent flow and the inlet boundary implement corresponding space-resolved velocity and TKE profiles. To obtain the velocity and TKE trends, single-phase simulations of the gas flow in a parallelepiped channel with the cross-section corresponding to the injection domain have been carried out, and the resulting flow field and turbulence profiles have been mapped in the domain used for VOF simulations and used to set fully developed flow boundary conditions. Figure 2 shows the cross-flow initialization domain, highlighting the overlap between the single-phase domain to initialize the cross flow (clear color) and the domain used for the injection (yellow).

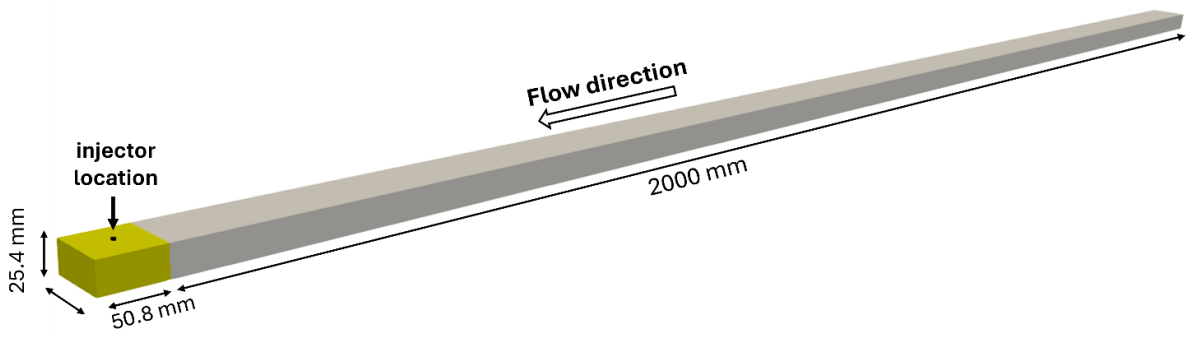

Figure 2. Representation of the CFD domains. The auxiliary domain used to initialize the gaseous flow field is reported in the clear color. The domain used for VoF simulation is shown in yellow, in which the flow field and turbulent profiles are mapped as fully developed.

Following preliminary simulations on its influence on the mass flow rate, a constant needle lift equal to 150 µm is set and the injector is initialized filled with air at ambient conditions to reproduce the dynamics of the internal flow. Distilled water is the working fluid, and it is injected in iso-thermal conditions. Other studies have already substituted UWS by distilled water due to their similar physical properties [36].

A summary of the operating conditions is reported in Table 1. The simulations reproduce the experimental conditions, in which both air and water are operated at ambient temperature Tamb = 298 K. The analysis of the results has been focused on the quasi-steady injection pattern, considering the needle opening and closing transients to be negligible for typical injection duration [37]. .To identify the quasi-steady behavior of the jet, needed to start collecting spray-representative data, the spray mass time history has been considered. After 2.5 ms of physical time (Figure 3) TIM stabilizes determining the quasi-steady operation in the chamber. Therefore, the data sampling time windows has been set to start at 2.5 ms from the start of the simulation.

Table 1. Summary of the simulation conditions with the characteristic boundary conditions.

Label	Injection pressure	Air cross-flow velocity
Cross-Flow 20 m/s	9 bar	20 m/s
Cross-Flow 10 m/s	9 bar	10 m/s
Quiescent	9 bar	0 m/s

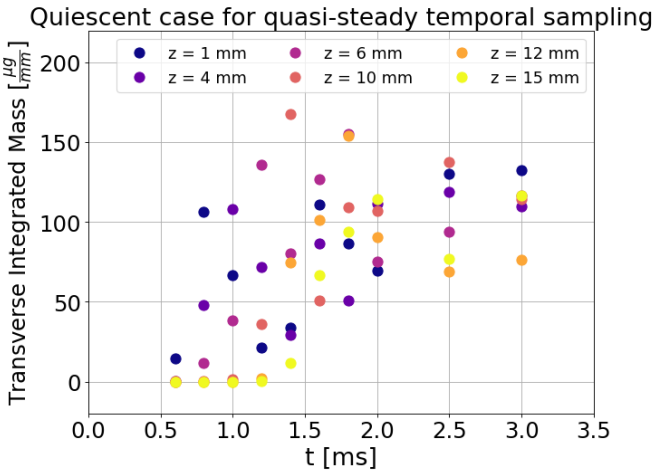

Figure 3. Transverse Integrated Mass (TIM) values for the quiescent case at several distances from the nozzle exit.

4. RESULTS

4.1. COMPARISON WITH EXPERIMENTAL DATA AND VALIDATION OF THE COMPUTATIONAL MODEL

The computational results have been compared with experimental data obtained using x-ray radiography by Moon et al. [18]. The simulated cross-flow conditions reproduce the experimental setup in terms of both injection and cross-flow conditions (Table 1) and the validation of the injector dynamics will be carried out in terms of projected liquid density profiles. In these cases, the incoming air flows in the X Axis, from positive to negatives values.

Droplet density projections provide useful information to detect where the intact sheet disintegrates into smaller droplets, and also for comparison with cross-flow density projections. 25 snapshots taken with a time-frequency of 50 kHz have been used to time-average the results. The averaged spray mass has been projected along the Y axis (Figure 1), and the area density is obtained from to the cross-sectional cell area. [18]

Figure 4 shows the comparison of the projected density between the two methods. Overall, good agreement is found as

the peak density values and location is matched. Values of 60 µg/mm2 are located near the nozzle exit for all the conditions tested, and in the boundaries of the spray, indicating how the hollow cone develops in both cases. Rapidly, projected density values decay as the liquid jet breaks into smaller droplets down to values close to 15 µg/mm2 for experimental means, and slightly higher for the CFD approach (~ 20 µg/mm2). The influence of the cross-flow momentum on the spray is well captured and highlighted by the deviation of the hollow jet. The coarser resolution of the projected density profile obtained from the simulations derives from the reduced number of sampling frames, due to the cost of the calculation and the slow nature of the jet penetration dynamics, which limits the sampling frequency of the simulations to generate average values.

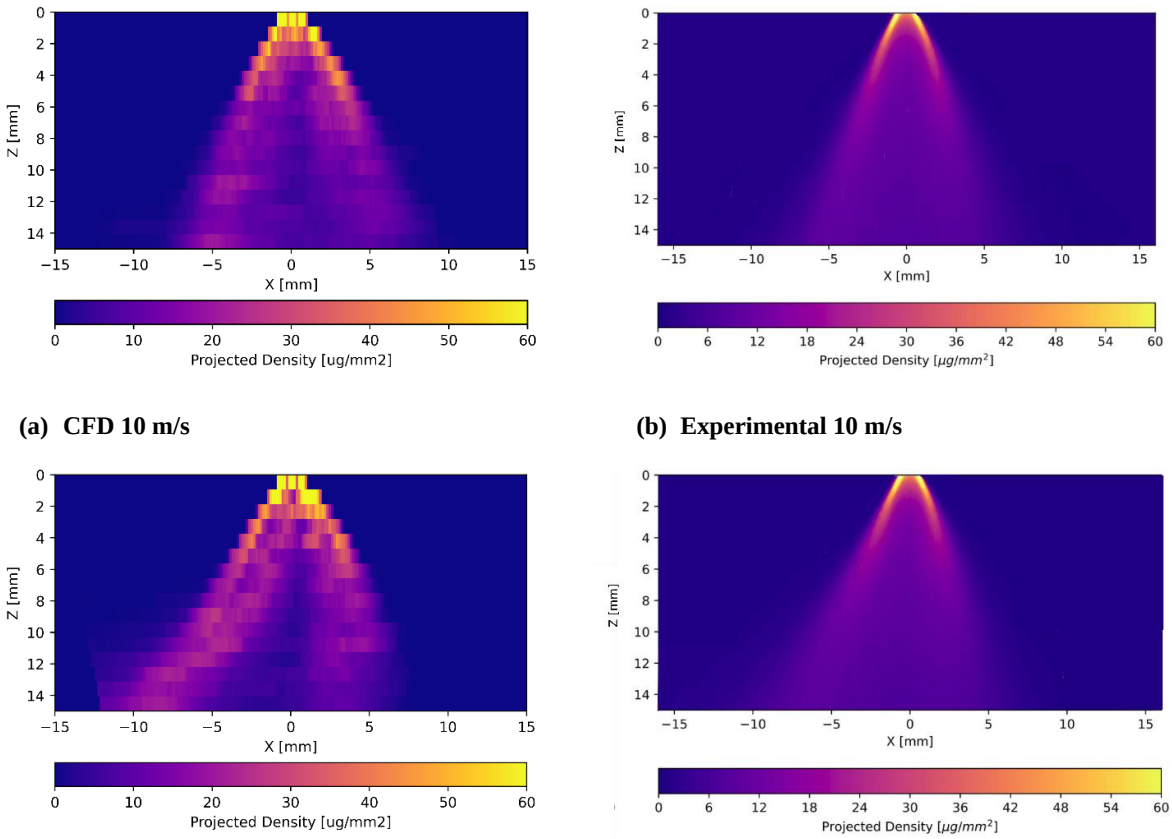

(a) CFD 10 m/s **(b) Experimental 10 m/s**

(c) CFD 20 m/s **(d) Experimental 20 m/s**

Figure 4. Comparison between experimental (b, d) [18] **and computational (a, c) results obtained for two cross-flow velocities. Gaseous cross-flow comes from positive X values (right to left).**

To provide a more insightful comparison between the two methods, density projection values have been extracted at several Z distances from the nozzle, and the outcomes have been plotted in **Figure 5**. Due to the limited amount of 3D datasets, a moving average filtering process has been applied to the computational results. In concordance with the

quantitative results previously shown, the projected density curves decay as the fluid penetrates the domain and breaks up. Figure 5 (a) and (d) include the result at 1 mm from the nozzle tip and show an overprediction of the projected density values and of the hollow cone width, which is due to the limited amount of valuable 3D datasets, which do not allow for fine spatial processing resolution. At higher distances from the nozzle, where the effect of the boundary layer starts to diminish, the injected liquid is more exposed to the bulk cross-flow velocity and the breakup of the primary jet generates a more statistically valuable distribution of the liquid, the curves show better agreement. The simulations are capable of capturing the effect of the cross flow on the spray, which maintains the hollow cone structure at 10 mm from the injector tip but is deviated from its initial axis.

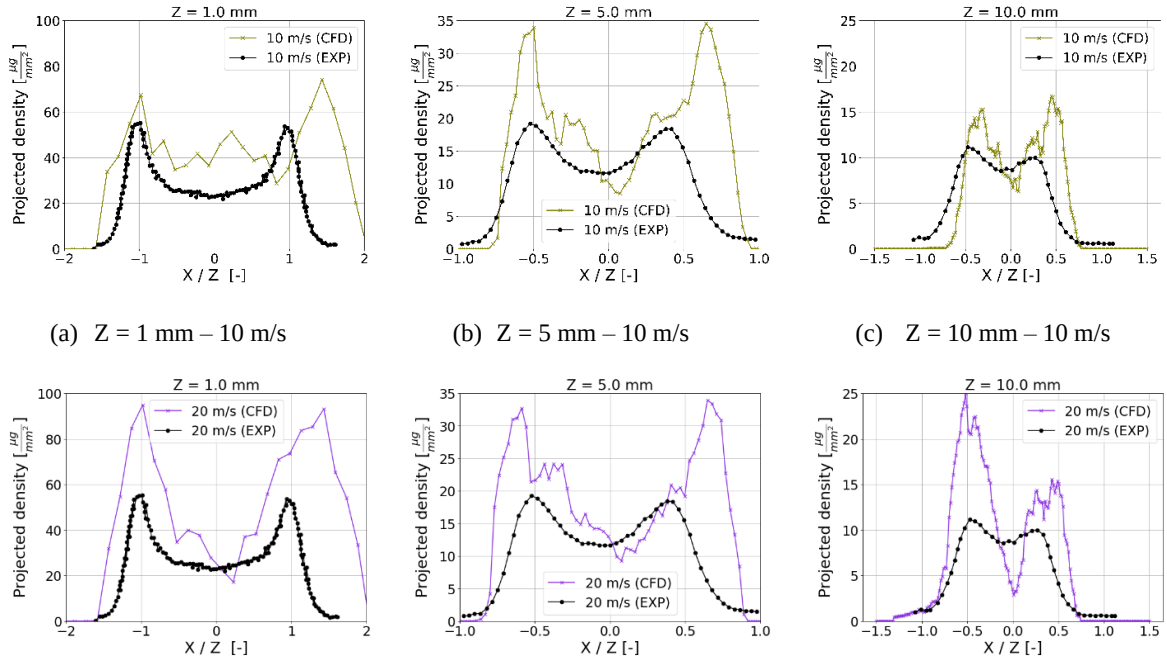

(a) Z = 1 mm – 10 m/s (b) Z = 5 mm – 10 m/s (c) Z = 10 mm – 10 m/s

(d) Z = 1 mm – 20 m/s (e) Z = 5 mm – 20 m/s (f) Z = 10 mm – 20 m/s

Figure 5. Comparison of the projected density profiles between the computational and experimental results [18] at specific distances from the UWS injector nozzle.

4.2 Hydraulic characterization of the nozzle flow

To quantify the swirling motion of the jet, the swirl number (SN) has been obtained at the nozzle exit interface. A transformation of the simulation coordinated from Cartesian to Cylindrical, preserving the Z-axis as the axial direction of the spray and obtaining radial and tangential components on the velocity on the planar section. The swirl number has been calculated according to Equation 7 for the three working conditions introduced. It represents the ratio of the axial flux of the angular momentum, to the axial flux of the axial momentum [38], [39], R the radius of the orifice, and U_a, U_s

and r the axial velocity, swirling velocity and distance to the nozzle center respectively. Similar SN is obtained for the three cross-flow conditions, with a mean value of SN = -0.173, indicating that the air flow rate is not affecting the spray dynamics prior to being injected into the domain. Note that the negative value of the SN represents a counter-clockwise swirling motion.

$$SN = \frac{\int \rho_L U_a U_s r dA_0}{R \int \rho_L U_a^2 dA_0} \tag{7}$$

The velocity profile at the nozzle exit remains unaffected as observed in the SN calculation for the three velocities, therefore, the swirl to hollow cone dynamics have been described based on the 20 m/s working condition. Figure 6-b shows the velocity components at two sections of the nozzle exit (Figure 6-a), showing the strength of the swirling motion. Note that the magnitude of the velocities has been obtained, and a positive value is shown for the swirling component although SN indicates a counter-clockwise direction. At Section 1 is a certain radial velocity component as the fluid coming from the injector channels are being forced against the nozzle walls. For the same reason, the swirling velocity component that has built up is larger than the radial component. At Section 2, there is a decrease in the axial velocity of almost 1 m/s from section. The fluid at this section has already detached from the nozzle walls as stated by the calculated Area Coefficient Ca=0.54, which is determined as the ratio of the effective area Aeff of the liquid jet and the geometric area Ageom of the nozzle. The effective area is determined as a function of the momentum $\dot{M}$ and the mass flow rate $\dot{M}$ of the liquid phase at the exit at Section 2 ($A_{eff} = \dot{m}^2/\rho_{liq}\,\dot{M}$) without assuming any specific flow topology. For that reason, there is a significant momentum (~10 m/s) transfer from the swirling component (built due to the wall presence) in Section 1 towards the radial component as it no longer has the nozzle wall as a restrictor, showing a lower swirling velocity in the region where the fluid has detached from the nozzle walls. Based on that increase on the radial velocity component, the hollow cone will enlarge once in the channel until the shear stresses of the incoming gas deforms the annular shape.

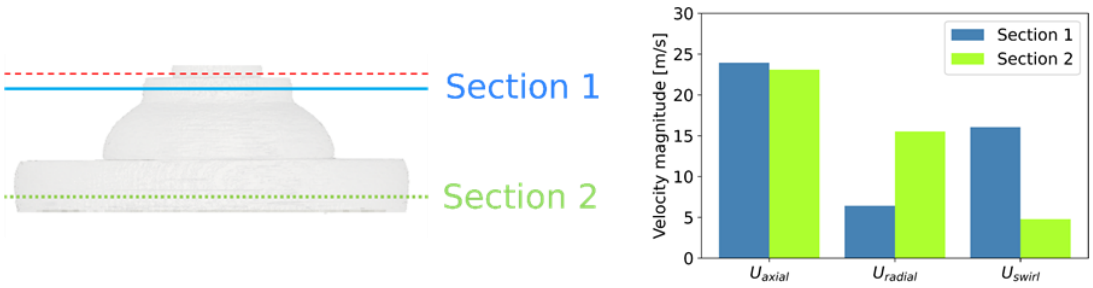

Figure 6. Velocity components obtained at the nozzle exit in the 20 m/s cross-flow simulation.

Momentum ratio (Equation 8) has also been obtained based on the spray-to-cross flow conditions (Table 2). From both cross-flow conditions, the injected fluid possesses considerably higher momentum than the one of the gas cross-flow at any of the two air velocity conditions. For the low cross-flow velocity case (10 m/s), the jet will be affected by the air until the jet has fully developed, and the liquid sheet has been severely affected by the instabilities and the sheet thinning.

$$J = \frac{\rho_j u_j^2}{\rho_\infty u_\infty^2} \tag{8}$$

Table 2. Momentum Ratio values for the three working conditions.

Case	Momentum Ratio
Quiescent	[-]
10 m/s	7567
20 m/s	1891

4.1 Breakup Dynamics

The typology of the wave instabilities introduced on the sheet depends on the gas Weber (We) number. A critical Weber number is established at We_c = 27/16 [40], and it represents a threshold separating long- and short-wave growth processes. The thickness of the liquid sheet (Equation 9) has been used as the characteristic length of the gas We number (Equation 10), where t_0, d_0 and C_a represent the sheet thickness, nozzle diameter and the area coefficient. For the three simulations, an area coefficient of 0.54 has been obtained, giving an initial thickness of 77 μm, and a subsequent We number of 0.73, which determines a long-wave growth regime.

$$t_0 = \frac{d_0\left(1 - \sqrt{1 - C_a}\right)}{2} \tag{9}$$

$$We_g = \frac{\rho_g u_l^2 t_0}{2\sigma} \tag{10}$$

This behavior is confirmed by the characteristic Reynolds number based on the sheet thickness and the Ohnesorge number, which define a breakup regime map [23]. Figure 7 shows that the liquid jet behaves according to the First Wind Induced regime, in which axisymmetric oscillations are caused by the relative jet velocity and the viscosity effects.

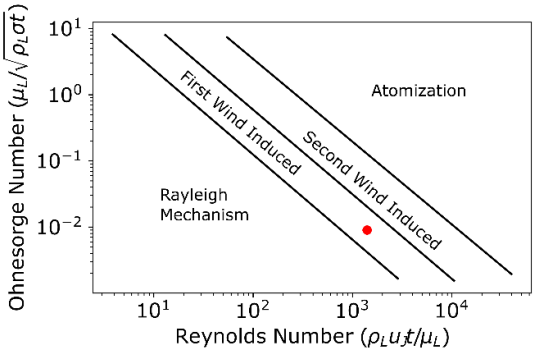

Figure 7. Reynolds-Ohnesorge chart of the pressure-swirl injector of interest.

Figure 8 shows a temporal snapshot of the spray morphology for the three injection conditions. The aerodynamic instabilities appear once the liquid is injected into the channel and are present until the core region breaks up into ligaments and droplets. To differentiate the liquid phase that belongs to the intact sheet and the broken-up droplets, a connectivity-based algorithm has been developed. First, the liquid phase has been separated from the gas phase using the volumetric void fraction scalar according to a threshold $\alpha = 0.6$. The algorithm then determines the connectivity between adjacent cells that fulfil the void fraction condition to label liquid clusters. After computing the volume of each cluster, they are separated from the initial sheet structure. Sudden atomization is captured by the simulations, with a complete breakup of the injected liquid sheet.

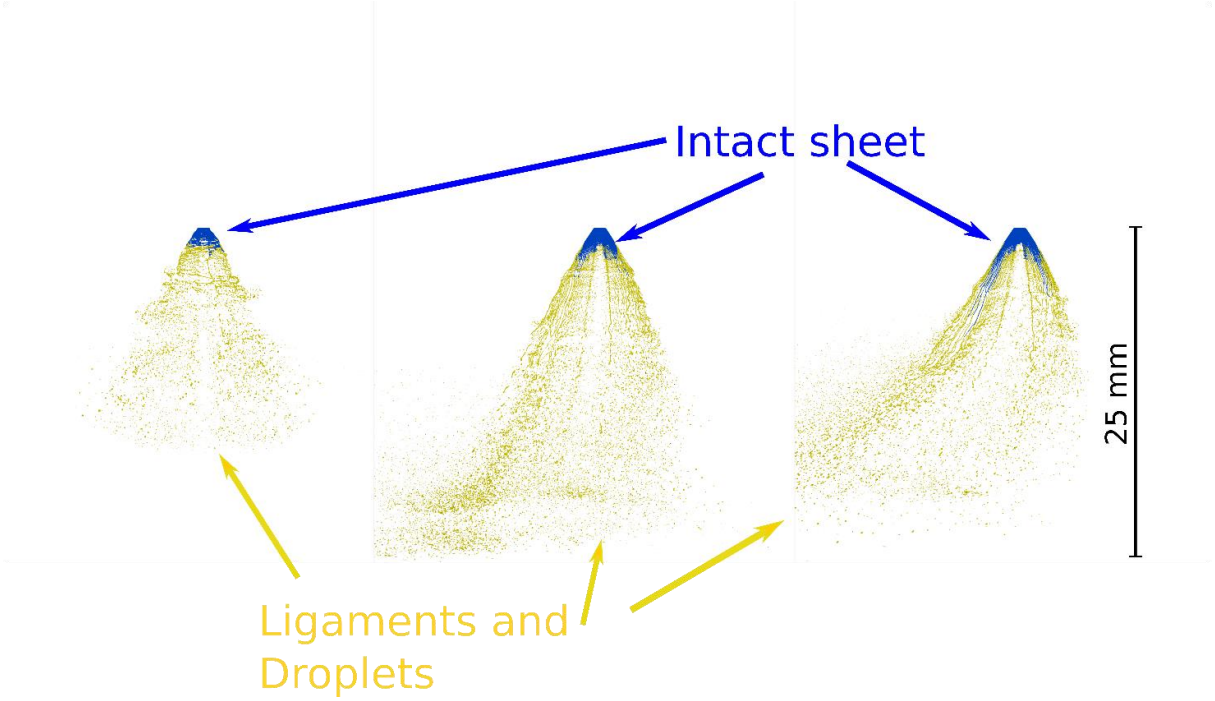

Figure 8. Representation of the liquid phase at a temporal snapshot obtained at 2.0 ms for the Quiescent (left), 10 m/s (middle) and 20 m/s (right) simulations.

Figure 9 shows the average mass ratio calculated in quasi-steady jet conditions, of the injected liquid that either belongs to the intact sheet or the droplets and ligaments for the three working conditions. For the quiescent case, at 1.5 mm from the nozzle location, the aerodynamic instabilities are already overcoming the surface tension forces, and slightly below 20% of the mass at that point is already part of the droplets and ligaments. At 2 mm, the mass contributions are inverted, showing that the intact sheet mass represents only 20% of the total liquid mass in that section. Farther downstream, the intact sheet carries negligible mass, indicating that almost the whole injected spray has undergone primary breakup by 2 mm. The cross-flow cases show that the instabilities are dampened by increasing the velocity of the gas and this dynamic delays the jet breakup, showing that until 5 mm and 6 mm for the 10 and 20 m/s respectively, the liquid core has not fully undergone the primary breakup phenomena. The full breakup location in this study corresponds to the axial location at which 95% of the total liquid mass is detached from the intact sheet. Intact length values have been included in Table 3.

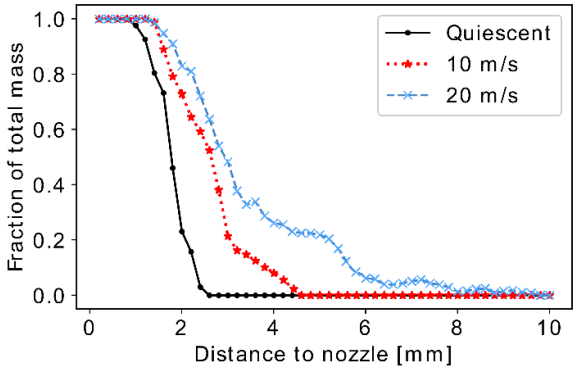

Figure 9. Representation of the mass fraction belonging to the intact sheet and the droplets/ligaments in quasi-steady conditions.

Table 3. Intact Length values for the three working conditions.

Working condition	**Intact Length**
Quiescent	1.05 mm
10 m/s	1.47 mm
20 m/s	1.58 mm

Moreover, the spray sheet thickness has been computed from the nozzle exit to assess at which value it reaches critical conditions and to detect where primary breakup takes place. Thickness values have been obtained by processing the volumetric void fraction profiles along a slice normal to the Y- direction, as shown in Figure 10. The obtained profiles are reported in in Figure 11, comparing the effect of the cross-flow. The injection into quiescent conditions shows a faster wave growth compared to the thickness evolution of the 10 and 20 m/s cross-flow conditions. The modification of the spray sheet thickness in the quiescent condition corresponds to the dilatational wave growth which rapidly leads to breakup. The simulations with 10 and 20 m/s cross-flow velocities only reach critical conditions after 2 mm from the nozzle. Incoming gas flow reduces the wave growth rate, although the sheet thickness decreases. The pressure distribution of the gas phase in the near-nozzle region differs from the quiescent and the cross-flow conditions. A high-pressure region is formed in quiescent conditions due to the force balancing between the surface tension forces and the aerodynamic forces, causing a static pressure distribution around the liquid jet. On the other hand, at 20 m/s, there is a local pressure drop caused by the incoming gas filling the empty zones of the nozzle (C_a = 0.54), and a consequent velocity rise due to the Venturi effect. This pressure drop homogenises the static pressure distribution that is induced by the force balance

previously mentioned, damping the instability growth and delaying the breakup.

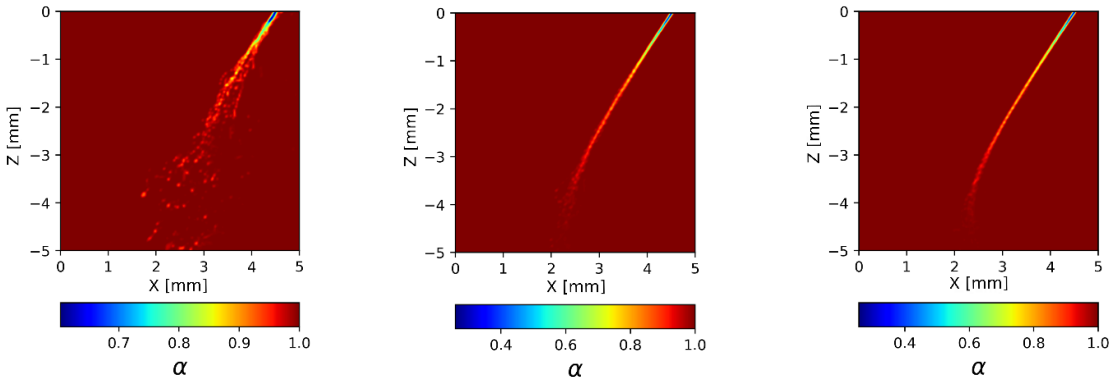

(a) Quiescent (b) 10 m/s (c) 20 m/s

Figure 10. Representation of the volumetric void fraction of the liquid sheet for the three simulations performed.

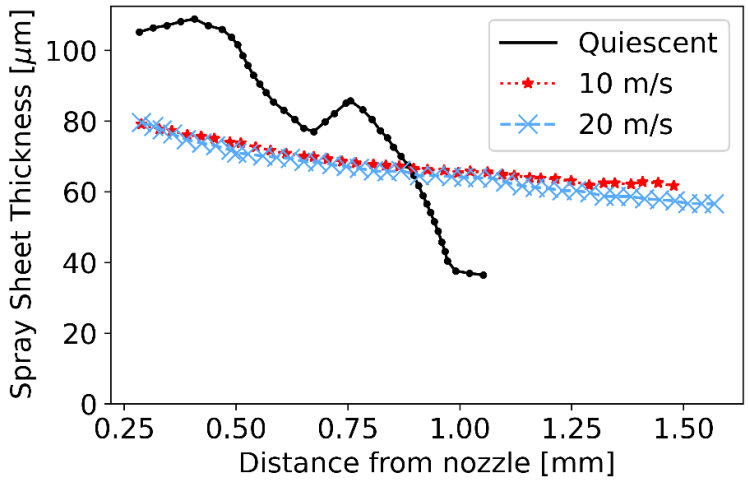

Figure 11. Spray sheet thickness comparison for the three simulations.

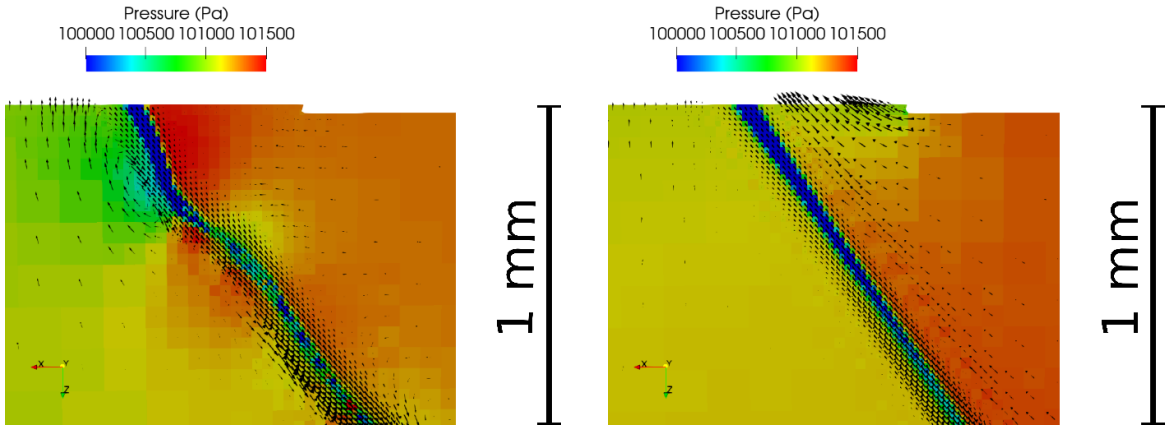

(a) Quiescent (b) 20 m/s

Figure 12. Y-Normal view of the pressure distribution and velocity vectors for the quiescent case and the 20m/s case in the near nozzle region.

The outcomes of the droplet breakup phenomena can be assessed by obtaining the Probability Density Functions (PDF) of the droplet diameters at several axial locations from the nozzle exit. Results are included in Figure 13. For the quiescent case, no significant changes are observed, indicating that the droplets formed at a distance of 1 mm are representative of the primary breakup distribution. From there, PDF curves are slightly skewed towards smaller diameters, indicating that the ligaments formed from the primary breakup have later separated into smaller droplets. It must be noted that the reported PDF are representative only of the detached liquid, and therefore, in the presence of partial breakup in the vicinity of the injector nozzle, the PDF is not representative of the total liquid mass present at the sampling plane. In fact, when it comes to the 10 and 20 m/s droplet diameter PDF curves, significant differences are observed between the closest sampling plane to the injector tip (1 mm) and the two downstream locations. According to the spray thickness results and the evolution of the spray mass located within the liquid core region, at a distance of 1 mm, the spray at cross-flow conditions has not fully undergone primary breakup, and therefore the droplet distribution is not representative of the complete atomization process. At 5 mm from the injector tip, a more representative distribution is found for both cases and, according to Figure 9, the primary breakup has already happened, and most of the injected mass belongs to detached droplets. There is no significant change at a farther distance (10 mm), indicating that secondary breakup phenomena are negligible at the studied test conditions. Figure 14 summarizes the spray PDF characteristics at 10 mm from the injection tip. A gradual shift of the PDF curve towards smaller diameters is observed with increasing cross-flow velocity. This shows that, although the intact length increases with increasing velocities for this working range, the shear stresses induced by the cross-flow reduce the droplet diameter as a result of the breakup of the spray sheet at relative large cross-

flow velocities. Other studies have assessed secondary breakup for UWS sprays [41] and resulted in the lack of such atomization due to the low Weber number of the liquid droplets. In addition, the Weber number of each of the formed droplets has been obtained and represented through a We-Re chart (Figure 15). Although all three conditions exhibit compatible We-Re trends, the quiescent condition shows a maximum We = 2, which is greatly smaller than the critical value of We = 12 that determines relevant presence of secondary breakup [23].

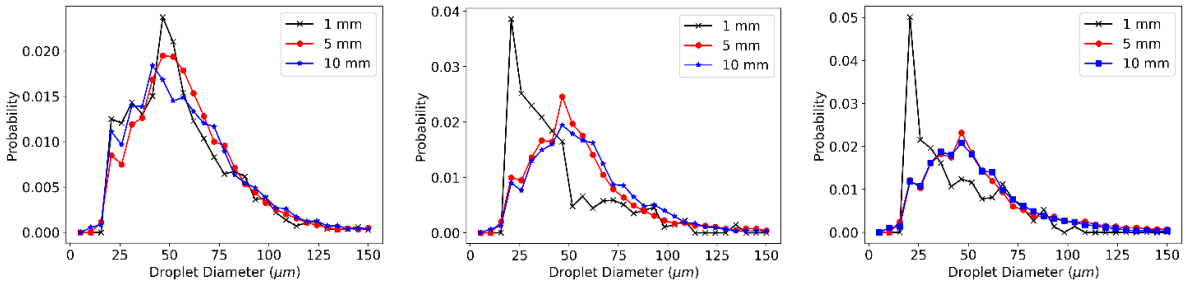

(c) Quiescent (d) 10 m/s (e) 20 m/s

Figure 13. PDF of diameter of the detached droplets at three distances from the nozzle for the three cases simulated.

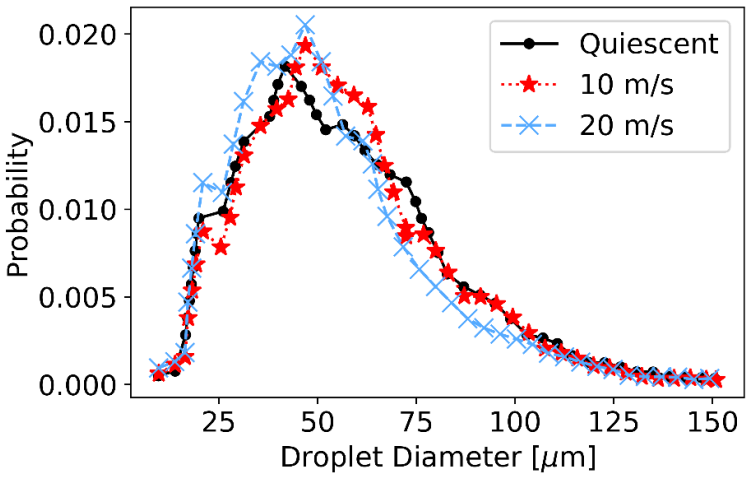

Figure 14. Comparison of droplet diameter PDF at a distance of 10 mm from the nozzle exit.

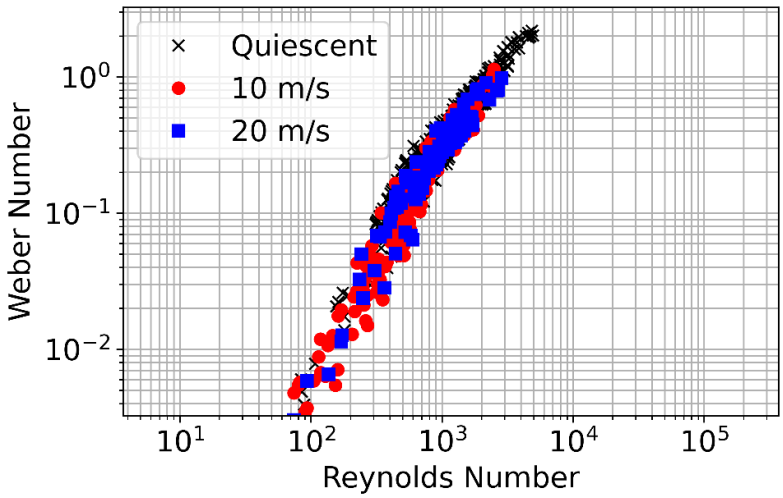

Figure 15. Reynolds-Weber number chart for the three working conditions calculated.

The kinematics of the liquid droplets have been assessed and reported in Figure 16. A clear momentum dissipation effect is visible for the quiescent case (Figure 16a), leading to radial peak velocities of 5 m/s at 10 mm from the nozzle. The same trend is followed with the axial velocity component (Figure 17a). In the cross-flow conditions, the dissipation of the liquid momentum is less abrupt, and the droplets report radial acceleration as a result of the interaction with the gaseous flow. This effect is clearer at higher gas velocities (20 m/s), as the radial velocity PDF peak is consistent between 5 mm and 10 mm. At high cross-flow velocities, there is a greater reduction on the axial velocity compared to the 10 m/s and quiescent simulations due to the momentum exchange. This gives information on how the relatively high cross-flow velocities diminish the chance of wall impingement of the formed droplets, but has a minor effect of the atomization dynamics.

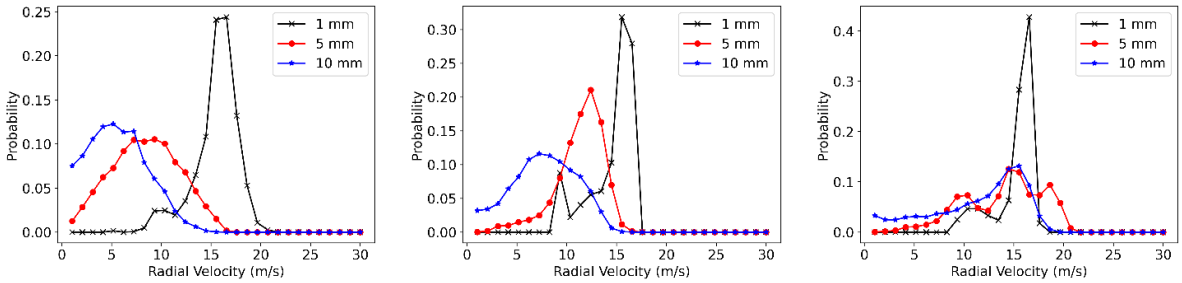

(a) Quiescent (b) 10 m/s (c) 20 m/s

Figure 16. PDF of droplet radial velocity at three distances from the nozzle for the three cases simulated.

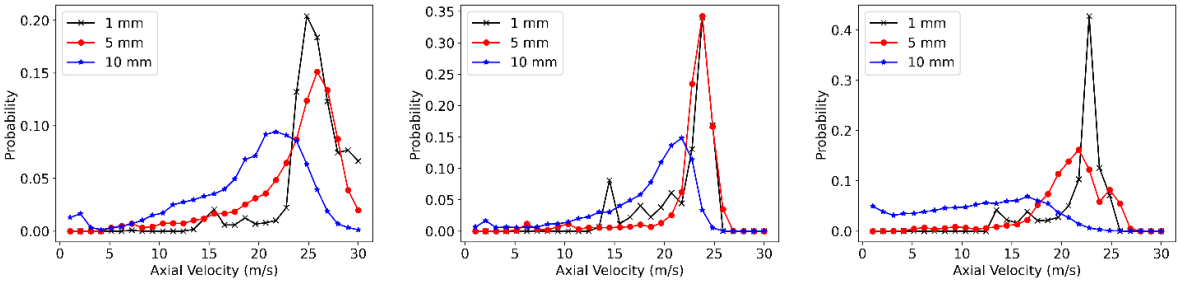

(a) Quiescent (b) 10 m/s (c) 20 m/s

Figure 17. PDF of droplet axial velocity at three distances from the nozzle for the three cases simulated.

4. CONCLUSIONS

The present work proposes a computational model to predict and characterize the primary breakup of a commercially available pressure-swirl atomizer for NOx after-treatment purposes. A Volume-Of-Fluid approach has been employed to model both liquid and gas phases. The model has been validated against experimental data, and the effect of the air-flow rate velocity on the spray formation has been assessed. The major results can be summarized as follows:

- The CFD model is capable of capturing the effect of the gaseous cross-flow on the fluid density profiles of the injected liquid, and the results have been validated against experimental data acquired using x-ray radiography. The simulations show an over-prediction of the local values of the projected density, which reduces at locations farther from the injector tip.
- The swirling-to-hollow cone dynamics are reproduced, showing the momentum transfer from the swirl component of the velocity towards the radial component once the fluid leaves the injector. The swirl number has been quantified, showing the strength of the swirling motion on the injector.
- The breakup of the liquid has been analysed, locating the spray dynamics under the first wind-induced regime. Intact Length values have been extracted indicating that increasing gas cross-flow velocities determine longer primary breakup lengths, due to local pressure drops generated by the incoming gas flow. Sheet thickness has been assessed, and in agreement with the Intact Length values, injection in quiescent atmosphere shows instabilities of the liquid sheet closer to the nozzle tip, when compared to cross-flow simulations.
- Probability Density Functions for the droplet size have been obtained, showing that, for the 10 m/s and 20 m/s cross flow velocity cases, breakup has not fully occurred at 1 mm from the nozzle. No significant breakup occurs

between 5 and 10 mm from the nozzle. The case of 20 m/s of cross-flow velocity shows smaller droplets than the other working conditions, the benefits of the cross-flow velocity on the spray breakup process while increasing intact length values. No secondary breakup is observed according to the Weber number of the detached droplets.

- Velocity PDF shows the effect of the momentum transfer with the incoming flow-rate. Wider radial velocity distributions are reported for increasing cross-flow velocity. With respect to axial velocity, there is significant reduction in the 20 m/s cross-flow velocity due to the momentum transfer between the phases.

The proposed Volume-Of-Fluid model allows for prediction the injection process of UWS under several working conditions, and to assess the primary breakup of the injected fluid. This study represents an initial step towards the characterization of the injection and breakup dynamics of low pressure-driven sprays for deNOx applications, with the goal of informing DDM Lagragian-Eulerian spray models through direct assignment of realistic droplet diameter PDFs or static one-way coupling between VoF results and Lagrangian spray parcels, to be used for system design and optimization workflows.

5. ACKNOWLEDGEMENTS

The submitted manuscript has been created by UChicago Argonne, LLC, Operator of Argonne National Laboratory ("Argonne"). Argonne, a U.S. Department of Energy Office of Science laboratory, is operated under Contract No. DE-AC02-06CH11357. The U.S. Government retains for itself, and others acting on its behalf, a paid-up nonexclusive, irrevocable worldwide license in said article to re- produce, prepare derivative works, distribute copiesto the public, and perform publicly and display publicly, by or on behalf of the Government.

We gratefully acknowledge Siddiq Khan and Gurpreet Singh at DOE's Office of Vehicle Technologies, Office of Energy Efficiency and Renewable Energy for funding this activity. We thank the computing resources provided on Bebop, a high-performance computing cluster operated by the Laboratory Computing Resource Center at Argonne, and Convergent Science Inc. for providing CONVERGE CFD software licenses and technical support. The experimental measurements presented in this work were obtained at the 7-BM beamline at the Advanced Photon Source (APS) at Argonne. Use of the APS is supported by DOE under Contract No. DE-AC02-06CH11357.

2. REFERENCES

[1] ACEA, "Vehicles in use in Europe 2022," 2022.

[2] R. D. Reitz *et al.*, "IJER editorial: The future of the internal combustion engine," *International Journal*

of Engine Research, vol. 21, no. 1, p. 146808741987799, 2019, doi: 10.1177/1468087419877990.

[3] I. A. Reşitolu, K. Altinişik, and A. Keskin, "The pollutant emissions from diesel-engine vehicles and exhaust aftertreatment systems," *Clean Technol Environ Policy*, vol. 17, no. 1, pp. 15–27, 2015, doi: 10.1007/s10098-014-0793-9.

[4] A. Dimaratos, Z. Toumasatos, S. Doulgeris, G. Triantafyllopoulos, A. Kontses, and Z. Samaras, "Assessment of CO2 and NOx Emissions of One Diesel and One Bi-Fuel Gasoline/CNG Euro 6 Vehicles During Real-World Driving and Laboratory Testing," *Front Mech Eng*, vol. 5, 2019, doi: 10.3389/fmech.2019.00062.

[5] A. C. Lewis, " Optimising air quality co-benefits in a hydrogen economy: a case for hydrogen-specific standards for NO x emissions ," *Environmental Science: Atmospheres*, vol. 1, no. 5, pp. 201–207, 2021, doi: 10.1039/d1ea00037c.

[6] M. Nozari, M. Eidiattarzade, S. Tabejamaat, and B. Kankashvar, "Emission and performance of a micro gas turbine combustor fueled with ammonia-natural gas," *International Journal of Engine Research*, p. 14680874211005052, May 2021, doi: 10.1177/14680874211005052.

[7] S. Ko *et al.*, "NOx emissions from Euro 5 and Euro 6 heavy-duty diesel vehicles under real driving conditions," *Energies (Basel)*, vol. 13, no. 1, pp. 1–13, 2020, doi: 10.3390/en13010218.

[8] R. Sala, P. Bielaczyc, and M. Brzezanski, "Concept of Vaporized Urea Dosing in Selective Catalytic Reduction," *Catalysts* , vol. 7, no. 10. 2017. doi: 10.3390/catal7100307.

[9] S. D. Yim *et al.*, "Decomposition of Urea into NH3 for the SCR Process," *Ind Eng Chem Res*, vol. 43, no. 16, pp. 4856–4863, Aug. 2004, doi: 10.1021/ie034052j.

[10] M. Li, Y. Zhang, J. Yang, X. Liu, Z. Li, and Q. Zhang, "Investigation on the urea deposit formation and thermal decomposition characteristics in the SCR aftertreatment system of a diesel engine," *J Environ Sci (China)*, vol. 103, pp. 157–171, May 2021, doi: 10.1016/j.jes.2020.10.015.

[11] E. Abu-Ramadan, K. Saha, and X. Li, "Numerical modeling of the impingement process of urea-water solution spray on the heated walls of SCR systems," *SAE Technical Papers*, no. x, 2012, doi: 10.4271/2012-01-1301.

[12] F. Qian, L. Lü, T. Feng, and D. Yang, "Experimental and 3D, embedded modeling for diesel engine SCR deposit," *International Journal of Automotive Technology*, vol. 18, no. 2, pp. 219–227, Apr. 2017, doi: 10.1007/s12239-017-0021-9.

[13] A. Kalyankar, M. Blessinger, A. Munnannur, and Z. G. Liu, "Impact of Choice of Spray Inputs on Simulations of Urea-Based Selective Catalytic Reduction Systems," *SAE Int J Engines*, vol. 13, no. 5, pp. 685–703, 2020, doi: 10.4271/03-13-05-0043.

[14] Ł. J. Kapusta, M. Sutkowski, R. Rogóż, M. Zommara, and A. Teodorczyk, "Characteristics of Water and Urea–Water Solution Sprays," *Catalysts* , vol. 9, no. 9. 2019. doi: 10.3390/catal9090750.

[15] G. Bracho, L. Postrioti, A. Moreno, and G. Brizi, "Experimental study of the droplet characteristics of a SCR injector spray through optical techniques," *International Journal of Multiphase Flow*, vol. 135, p. 103531, Feb. 2021, doi: 10.1016/j.ijmultiphaseflow.2020.103531.

[16] L. Nocivelli, G. Montenegro, Y. Liao, P. D. Eggenschwiler, J. Campbell, and N. Rapetto, "Modeling of Aqueous Urea Solution injection with characterization of spray-wall cooling effect and risk of onset of wall wetting," in *Energy Procedia*, Dec. 2015, vol. 82, pp. 38–44. doi: 10.1016/j.egypro.2015.11.880.

[17] Y. Liao, R. Furrer, P. Dimopoulos Eggenschwiler, and K. Boulouchos, "Experimental investigation of the heat transfer characteristics of spray/wall interaction in diesel selective catalytic reduction systems," *Fuel*, vol. 190, pp. 163–173, Feb. 2017, doi: 10.1016/j.fuel.2016.11.035.

[18] T. X. Radiography, C. Y. Moon, Q. Peng, B. A. Sforzo, A. L. Kastengren, and C. F. Powell, "Near-nozzle Density of Pressure-swirl Atomizing Sprays in a Crossflow usingTime-resolved X-ray Radiography," in *ILASS Americas*, 2022.

[19] R. Payri, G. Bracho, P. Martí-Aldaraví, and J. Marco-Gimeno, "Computational Study of Urea–Water Solution Sprays for the Analysis of the Injection Process in SCR-like Conditions," *Ind Eng Chem Res*, vol. 59, no. 41, pp. 18659–18673, Oct. 2020, doi: 10.1021/acs.iecr.0c02494.

[20] A. Varna, K. Boulouchos, A. Spiteri, P. Dimopoulos Eggenschwiler, and Y. M. Wright, "Numerical Modelling and Experimental Characterization of a Pressure-Assisted Multi-Stream Injector for SCR Exhaust Gas After-Treatment," *SAE Int J Engines*, vol. 7, no. 4, pp. 2012–2021, 2014, doi: 10.4271/2014-01-2822.

[21] A. Varna, A. C. Spiteri, Y. M. Wright, P. Dimopoulos Eggenschwiler, and K. Boulouchos, "Experimental and numerical assessment of impingement and mixing of urea–water sprays for nitric oxide reduction in diesel exhaust," *Appl Energy*, vol. 157, pp. 824–837, 2015, doi: 10.1016/j.apenergy.2015.03.015.

[22] R. Payri, G. Bracho, P. Martí-Aldaraví, and J. Marco-Gimeno, "Numerical Analysis of Urea to Ammonia Conversion in Automotive Selective Catalytic Reduction Realistic Conditions," *Ind Eng Chem Res*, vol.

60, no. 39, pp. 14329–14340, 2021, doi: 10.1021/acs.iecr.1c02627.

[23] A. H. Lefebvre and V. G. McDonell, *Atomization and sprays*, Second. Boca Raton, FL: Press, CRC, 2017. doi: 10.1201/9781315120911.

[24] C. Chen and Z. Tang, "Investigation of the spray formation and breakup process in an open-end swirl injector," *Sci Prog*, vol. 103, no. 3, pp. 1–19, Jul. 2020, doi: 10.1177/0036850420946168.

[25] J. Ishimoto, F. Sato, and G. Sato, "Computational prediction of the effect of microcavitation on an atomization mechanism in a gasoline injector nozzle," *J Eng Gas Turbine Power*, vol. 132, no. 8, May 2010, doi: 10.1115/1.4000264.

[26] R. Payri, G. Bracho, P. Marti-Aldaravi, and J. Marco-Gimeno, "Mixture Model Approach for the Study of the Inner Flow Dynamics of an AdBlue Dosing System and the Characterization of the Near-Field Spray." SAE International, 2021.

[27] W. Edelbauer, F. Birkhold, T. Rankel, Z. Pavlović, and P. Kolar, "Simulation of the liquid break-up at an AdBlue injector with the volume-of-fluid method followed by off-line coupled Lagrangian particle tracking," *Comput Fluids*, vol. 157, pp. 294–311, 2017, doi: 10.1016/j.compfluid.2017.09.003.

[28] Convergent Science, Ed., *CONVERGE 3.0 Manual*. Middleton, 2019.

[29] R. I. Issa, "Solution of the implicitly discretised fluid flow equations by operator-splitting," *J Comput Phys*, vol. 62, no. 1, pp. 40–65, 1986, doi: 10.1016/0021-9991(86)90099-9.

[30] C. M. Rhie and W. L. Chow, "Numerical study of the turbulent flow past an airfoil with trailing edge separation," *AIAA Journal*, vol. 21, no. 11, pp. 1525–1532, Nov. 1983, doi: 10.2514/3.8284.

[31] G. L. G. Sleijpen and D. R. Fokkema, "BiCGstab for linear equations involving unsymmetric matrices with complex spectrum.," *ETNA. Electronic Transactions on Numerical Analysis [electronic only]*, vol. 1, pp. 11–32, 1993, [Online]. Available: http://eudml.org/doc/118652

[32] T. Waclawczyk and T. Koronowicz, "Modeling of the wave breaking with CICSAM and HRIC high resolution schemes," *undefined*, 2006.

[33] M. Germano, U. Piomelli, P. Moin, and W. H. Cabot, "A dynamic subgrid-scale eddy viscosity model," *Physics of Fluids A: Fluid Dynamics*, vol. 3, no. 7, pp. 1760–1765, Jul. 1991, doi: 10.1063/1.857955.

[34] H. Werner and H. Wengle, "Large-Eddy Simulation of Turbulent Flow Over and Around a Cube in a Plate Channel BT - Turbulent Shear Flows 8," 1993, pp. 155–168.

[35] Z. Yue, M. Battistoni, and S. Som, "Spray characterization for engine combustion network Spray G

injector using high-fidelity simulation with detailed injector geometry," *International Journal of Engine Research*, vol. 21, no. 1, pp. 226–238, 2020, doi: 10.1177/1468087419872398.

[36] A. Spiteri, A. Srna, and P. Dimopoulos Eggenschwiler, "Characterization of sprays of water and urea-water solution from a commercial injector for SCR DeNOx applications," in *13th Stuttgart international symposium. Automotive and engine technology. Volume 1*, 2013, pp. 193–201.

[37] R. Payri, G. Bracho, J. Gimeno, and A. Moreno, "A Methodology for the hydraulic characterization of a Urea-Water Solution injector by means of Spray Momentum Measurement," in *29th European Conference on Liquid Atomization and Spray Systems*, 2019, no. 2-4 September.

[38] M. di Martino, D. Ahirwal, and P. L. Maffettone, "Three-dimensional computational fluid dynamics simulation of the hollow-cone spray process: The stability of the conical liquid sheet," *Physics of Fluids*, vol. 33, no. 6, 2021, doi: 10.1063/5.0051309.

[39] C. E. Morris, D. M. O'Doherty, A. Mason-Jones, and T. O'Doherty, "Evaluation of the swirl characteristics of a tidal stream turbine wake," *International Journal of Marine Energy*, vol. 14, pp. 198–214, 2016, doi: https://doi.org/10.1016/j.ijome.2015.08.001.

[40] P. K. Senecal, D. P. Schmidt, I. Nouar, C. J. Rutland, R. D. Reitz, and M. L. Corradini, "Modeling high-speed viscous liquid sheet atomization," *International Journal of Multiphase Flow*, vol. 25, pp. 1073–1097, 1999, doi: 10.1016/S0301-9322(99)00057-9.

[41] C. Bai, K. Liu, T. Zhao, and J. Liu, "Study on Spray Characteristics and Breakup Mechanism of an SCR Injector," *Applied Sciences (Switzerland)*, vol. 12, no. 18, 2022, doi: 10.3390/app12189387.